Anisotropy of the Fermi surface, Fermi velocity, many-body enhancement, and superconducting energy gap in Nb

G. W. Crabtree, D. H. Dye, D. P. Karim, and S. A. Campbell
Materials Science Division, Argonne National Laboratory, Argonne, Illinois 60439-4843

J. B. Ketterson
Department of Physics and Astronomy and Materials Research Center, Northwestern University, Evanston, Illinois 60201

(Received 5 June 1986)

The detailed angular dependence of the Fermi radius $\mathbf{k}_F$, the Fermi velocity $\mathbf{v}_F(\mathbf{k})$, the many-body enhancement factor $\lambda(\mathbf{k})$, and the superconducting energy gap $\Delta(\mathbf{k})$, for electrons on the Fermi surface of Nb are derived with use of the de Haas–van Alphen (dHvA) data of Karim, Ketterson, and Crabtree [J. Low Temp. Phys. **30**, 389 (1978)], a Korringa-Kohn-Rostoker parametrization scheme, and an empirically adjusted band-structure calculation of Koelling. The parametrization is a nonrelativistic five-parameter fit allowing for cubic rather than spherical symmetry inside the muffin-tin spheres. The parametrized Fermi surface gives a detailed interpretation of the previously unexplained κ, α', and α'' orbits in the dHvA data. Comparison of the parametrized Fermi velocities with those of the empirically adjusted band calculation allow the anisotropic many-body enhancement factor $\lambda(\mathbf{k})$ to be determined. Theoretical calculations of the electron-phonon interaction based on the tight-binding model agree with our derived values of $\lambda(\mathbf{k})$ much better than those based on the rigid-muffin-tin approximation. The anisotropy in the superconducting energy gap $\Delta(\mathbf{k})$ is estimated from our results for $\lambda(\mathbf{k})$, assuming weak anisotropy.

I. INTRODUCTION

Because of its high superconducting transition temperature (9.25 K), niobium plays a special role among the transition metals. In any attempt to achieve a quantitative, first-principles understanding of transition-metal superconductivity, Nb is the logical element for study because it displays large electron-phonon effects leading to high-T_c superconductivity. Most theoretical effort has focused on calculation of the transition temperature T_c and its variation across the transition series. However T_c is but a single number and a calculation might fortuitously reproduce the experimental value but otherwise give a poor representation of the overall problem. A quantity providing much greater experimental detail is the anisotropic electron-phonon enhancement factor $\lambda(\mathbf{k})$ defined through

$$\frac{|\mathbf{v}_{\text{band}}(\mathbf{k})|}{|\mathbf{v}_{\text{expt}}(\mathbf{k})|}=1+\lambda(\mathbf{k}) , \tag{1}$$

where $\mathbf{v}_{\text{band}}$ and $\mathbf{v}_{\text{expt}}$ are the band structure and the experimental quasiparticle (dressed) velocities, respectively. A first-principles theory which achieved full quantitative agreement with $\lambda(\mathbf{k})$ and T_c would have to be judged quite successful. In carrying out a program of this sort one must keep in mind that $\lambda(\mathbf{k})$ as defined above contains certain electron-electron contributions which are not adequately accounted for in a band-structure calculation, along with the electron-phonon effects. However, for Nb, with its high T_c, we may reasonably expect that the electron-electron effects are relatively less important than for some other transition metals.

Traditionally, most experimental information on λ has come from tunneling measurements. Since these have seldom been performed on single crystals, interest in $\lambda(\mathbf{k})$ has been lacking and the theory is usually formulated around the quantity $\alpha^2F(\omega)$, where anisotropic effects have already been averaged out. In addition to problems associated with polycrystalline averaging, the tunneling phenomenon itself is parametrized and little account of the direction and Fermi-surface-sheet dependence of the Fermi velocity is taken. Given this situation, experimental information on the sheet and direction dependence of $\lambda(\mathbf{k})$ should be welcome.

In recent years quantities measured in de Haas–van Alphen (dHvA) experiments have achieved a level of accuracy and completeness that allows specific information on $\lambda(\mathbf{k})$ and other electronic properties of interest to be derived.[1] To accomplish this, rather sophisticated Fermi-surface deconvolution (or inversion) programs are required along with a comparison of the derived Fermi velocities with those calculated using first-principles band-structure methods.[2]

Since it is anticipated that the results of this work may be of interest to those not ordinarily interested in the fine details of electronic structure, our methods for deducing the quasiparticle velocity will be briefly reviewed in this paper. Readers not interested in these details can skip Sec. II.

The experimental quantities measured in dHvA experiments are the angular dependences of the extremal cross-sectional area and cyclotron-effective mass. Both of these

quantities are averages of point properties of the Fermi surface around a cyclotron orbit. The problem of deconvoluting (or inverting) these orbital averages to deduce the point properties has commanded much interest. The most successful methods involve the parametrization of some band structure calculation scheme such as the Korringa-Kohn-Rostoker (KKR) or Green's-function method. Here one employs as disposable parameters the partial-wave scattering phase shifts characterizing the muffin-tin potential at the Fermi energy. Given a set of phase shifts one can calculate Fermi radius vectors and thus extremal cross-sectional areas. One can then vary the phase shifts until a weighted root-mean-square (rms) error between the calculated and measured areas is minimal.

By introducing the energy derivatives of the phase shifts as a second set of disposable parameters one can calculate the Fermi velocities which, when combined with knowledge of the Fermi radii, allows the cyclotron effective masses to be determined. One can choose these phase-shift energy derivatives so that a weighted rms error between the measured and calculated masses is minimal. This procedure allows, in principle, a complete determination of the Fermi surface and quasiparticle velocity from dHvA area and masses. The application of these techniques to noble metals has been quite successful.[3] Recently the relativistic form of this method, generalized to include nonspherically symmetric contributions to the muffin-tin potential, has been used to parametrize the Fermi surface of the transition metals Mo,[4] W,[4] Pt,[5] and Pd.[6,7] Preliminary nonrelativistic parametrizations of the Nb Fermi surface have also appeared.[8,9] A general review of the procedure is given in Ref. 2.

The availability of detailed and accurate Fermi radii allows a stringent test of the accuracy of modern first-principles band-structure-calculation methods. Given a potential, the techniques for self-consistently solving the band-structure problem are now highly developed and very accurate. However, the problem of just how to construct the proper one-electron potential is still not fully solved. A number of schemes exist and the agreement between measured and calculated Fermi-surface dimensions is generally within a few percent and sometimes considerably better. The situation with Fermi velocities is more complex since it is known that many-body effects reduce the dressed quasiparticle velocity $\mathbf{v}_{\text{expt}}$ relative to the band-structure velocity $\mathbf{v}_{\text{band}}$ through a quantity $\lambda(\mathbf{k})$ defined such that $\mathbf{v}_{\text{expt}}=\mathbf{v}_{\text{band}}/[1+\lambda(\mathbf{k})]$. Very little is known about the anisotropy of $\lambda(\mathbf{k})$, although its Fermi-surface average can be determined from a comparison of the densities of states determined from the electronic heat capacity and the band-structure calculation, or from superconducting tunneling measurements.

A determination of $\lambda(\mathbf{k})$ by comparing $\mathbf{v}_{\text{band}}(\mathbf{k})$ and $\mathbf{v}_{\text{expt}}(\mathbf{k})$ is only as good as the accuracy of the two velocities involved. For this reason it is best to initiate a program to examine $\lambda(\mathbf{k})$ in metals where the many-body effects are particularly large. Two such metals are Nb and Pd; in the former the electron-phonon mechanism dominates while in the latter the paramagnon or spin fluctuation mechanism is thought to be most important. Calculations of $\lambda(\mathbf{k})$ in Nb have been done by a number of groups[10–13] and will be compared with data to be presented here. The $\lambda(\mathbf{k})$ reported in this paper are determined by comparing the dHvA velocities with those calculated from a semiempirical band-structure calculation of Koelling[14] which was adjusted by artificially moving the p states relative to the s-d states to give an excellent overall agreement with the experimental radii. One might expect that this semiempirical band structure, since it yields a surface in excellent agreement with the experimental one, predicts band-structure velocities that are also quite accurate.

This paper is organized as follows. In Sec. II we briefly review the phase-shift parametrization technique. In Sec. III we present the Fermi radii and velocities in Nb determined by our procedure. The parametrization of the Fermi surface geometry is used to interpret the previously unexplained κ, α', and α'' orbits observed in dHvA experiments. The Fermi radii and velocities are numerically integrated to give the corresponding surface averaged properties, the number of carriers and densities of states, for each of the three sheets of the Fermi surface. In Sec. IV we present our results for $\lambda(\mathbf{k})$ and compare them with theoretical calculations based on the rigid muffin-tin and tight-binding approximations. Section V contains estimates of the anisotropy in the superconducting energy gap $\Delta(\mathbf{k})$ based on our values of $\lambda(\mathbf{k})$, assuming weak anisotropy.

II. THE PHASE-SHIFT PARAMETRIZATION TECHNIQUES

Since the KKR phase-shift parametrization technique has been discussed in detail in earlier publications[3,4] we will limit ourselves here to a brief outline. The KKR band-structure formalism reduces to the solution of a determinantal equation of the form

$$||A_{l,m;l',m'}-\delta_{l,m;l'm'}\sqrt{E}\,\cot\eta_l(E)||=0\ , \tag{2}$$

where the energy- and momentum-dependent quantities $A_{lm;l'm'}$ are the so-called "structure constants" which depend only on the crystal structure and lattice constant. The $\eta_l(E)$ are the energy-dependent muffin-tin scattering phase shifts which depend on the crystal potential and thus differ between metals. When considering a constant energy surface, e.g., the Fermi surface, the energy in Eq. (2) is fixed and, for a given direction $\mathbf{k}$, the magnitude $|\mathbf{k}|$ may be varied until the determinant vanishes. To facilitate the solution of Eq. (2) and to easily generate derivative information, it is better to regard the determinant as a matrix, $\overleftrightarrow{\mathrm{M}}$, one or more of whose eigenvalues, $\Lambda^{(i)}$, vanishes at a root. In the vicinity of the ith root we can expand $\Lambda^{(i)}(\mathbf{k})$

$$\Lambda^{(i)}(\mathbf{k}_F+\delta\mathbf{k})=\Lambda^{(i)}(\mathbf{k}_F)+\frac{\partial\Lambda^{(i)}}{\partial\mathbf{k}}\cdot\delta\mathbf{k}$$

and determine how great a shift $\delta\mathbf{k}$ in radius vector $\mathbf{k}$ is required to locate a value $\mathbf{k}_F$ which is on the surface. The required derivative is given by

$$\frac{\partial\Lambda^{(i)}}{\partial\mathbf{k}}=\mathbf{V}^{*(i)}\cdot\frac{\partial\overleftrightarrow{\mathbf{M}}}{\partial\mathbf{k}}\cdot\mathbf{V}^{(i)}\,, \tag{3}$$

an exact expression which follows from first-order perturbation theory. $\mathbf{V}^{(i)}$ is the eigenvector associated with the ith eigenvalue of the matrix $\overleftrightarrow{\mathbf{M}}$. The matrix elements $\partial\overleftrightarrow{\mathbf{M}}/\partial\mathbf{k}$ may be calculated by analytically differentiating the various structure constant sums and evaluating these in parallel with the sums for the structure constants themselves. In the same way other useful derivatives of the eigenvalues may be derived:

$$\frac{\partial\Lambda^{(i)}}{\partial\eta_l}=\mathbf{V}^{*(i)}\cdot\frac{\partial\overleftrightarrow{\mathbf{M}}}{\partial\eta_l}\cdot\mathbf{V}^{(i)}\,, \tag{4}$$

$$\left.\frac{\partial\Lambda^{(i)}}{\partial E}\right|_{\eta_l}=\mathbf{V}^{*(i)}\cdot\frac{\partial\overleftrightarrow{\mathbf{M}}}{\partial E}\cdot\mathbf{V}^{(i)}\,, \tag{5}$$

where the subscript η_l in Eq. (5) denotes that the phase shifts are held constant so that the derivative accounts only for the explicit dependence of the structure constants on energy. To include the implicit dependence of the eigenvalue on energy through the phase shifts, we use

$$\frac{\partial\Lambda^{(i)}}{\partial E}=\left.\frac{\partial\Lambda^{(i)}}{\partial E}\right|_{\eta_l}+\sum_l\frac{\partial\Lambda^{(i)}}{\partial\eta_l}\eta_l'\,, \tag{6}$$

where we define $\eta_l'\equiv d\eta_l/dE$. These expressions can be used to evaluate the Fermi velocities analytically:

$$\mathbf{v}_F\equiv\frac{1}{\hbar}\frac{\partial E}{\partial\mathbf{k}}=-\frac{1}{\hbar}\frac{\partial\Lambda^{(i)}/\partial\mathbf{k}}{\partial\Lambda^{(i)}/\partial E}\,, \tag{7}$$

where the full expression Eq. (6) is used for $\partial\Lambda^{(i)}/\partial E$.

The areas A and effective masses m^* are determined by numerical integration

$$A=\tfrac{1}{2}\int_0^{2\pi}k^2d\psi\,, \tag{8}$$

$$m^*=\frac{\hbar^2}{2\pi}\frac{\partial A}{\partial E}=\frac{\hbar^2}{2\pi}\int_0^{2\pi}\frac{k^2d\psi}{\mathbf{k}\cdot(\partial E/\partial\mathbf{k})}\,, \tag{9}$$

where $\mathbf{k}(\psi)$ is a radius vector in the plane of the orbit making an angle ψ with some convenient reference direction. To determine the phase shifts we minimize a quantity

$$\Delta_A^2=\frac{1}{N}\sum_{i=1}^{N}\left[\frac{A_i^{(\mathrm{calc})}-A_i^{(\mathrm{expt})}}{A_i^{(\mathrm{expt})}}\right]^2W_i\,, \tag{10}$$

where $A_i^{(\mathrm{calc})}$ and $A_i^{(\mathrm{expt})}$ are a selected set of calculated and experimental areas, N is the total number of areas fitted, and the W_i are weighting factors. Equation (10) is minimized with respect to the phase shifts η_l, which requires the derivatives

$$\frac{\partial A}{\partial\eta_l}=\int_0^{2\pi}\mathbf{k}\cdot\frac{\partial\mathbf{k}}{\partial\eta_l}d\psi\,, \tag{11}$$

where

$$\frac{\partial\mathbf{k}}{\partial\eta_l}=-\frac{\partial\Lambda^{(i)}/\partial\eta_l}{\partial\Lambda^{(i)}/\partial\mathbf{k}}\,. \tag{12}$$

Since the calculated areas are a nonlinear function of the phase shifts, the minimization proceeds by choosing some initial set of phase shifts (usually determined by a band-structure calculation), linearizing the equations resulting from the minimization condition, and iterating until a local minimum is found in the error functional. Starting from the band-structure values for η_l presumably insures that the minimum found is indeed global. To determine the parameters η_l', and thus the Fermi velocity, we minimize the following function with respect to η_l'

$$\Delta_M^2=\frac{1}{N}\sum_{i=1}^{N}\left[\frac{(\partial A_i^{(\mathrm{calc})}/\partial E)-(\partial A_i^{(\mathrm{expt})}/\partial E)}{\partial A_i^{(\mathrm{expt})}/\partial E}\right]^2W_i\,, \tag{13}$$

where

$$\frac{\partial A_i^{(\mathrm{calc})}}{\partial E}=\left.\frac{\partial A_i}{\partial E}\right|_{\eta_l}+\sum_l\frac{\partial A_i}{\partial\eta_l}\eta_l'\,. \tag{14}$$

This results in a strictly linear set of equations for η_l'. In addition to the band-structure contributions to η_l', we are also absorbing many-body effects (electron-phonon interaction, etc.) when we fit experimental effective masses. The legitimacy of such a procedure has not been examined theoretically to our knowledge; however, given the accuracy with which we are able to fit the highly enhanced masses of niobium, any errors involved in such an approximation are probably quite small. We offer some justification for this procedure in Sec. III C.

Once a set of phase shifts and their energy derivatives have been generated by fitting the areas and masses, the number of carriers $n(E)$ and density of states $N(E)$ of a given Fermi-surface sheet may be evaluated using

$$n(E)=\frac{2}{(2\pi)^3}V_k$$

and

$$N(E)=\frac{2}{(2\pi)^3}\frac{\partial V_k}{\partial E}\,,$$

where V_k and $\partial V_k/\partial E$ are the volume in k space and its energy derivative, respectively. The techniques for performing such integrations are outlined briefly in Appendix B.

III. CALCULATED RESULTS

Since the detailed experimental results for the extremal cross-sectional areas and cyclotron-effective masses in Nb

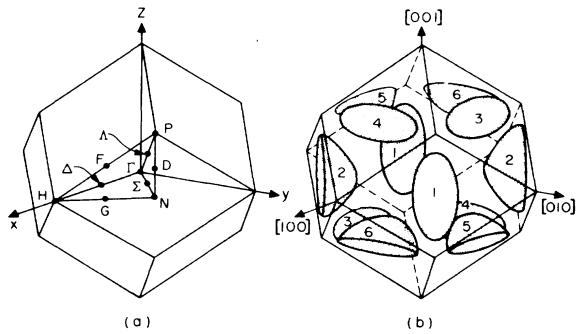

FIG. 1. (a) bcc Brillouin zone symmetry notation; (b) numbering system for the N-centered ellipsoid hole surface [after Mattheis (Ref. 17)].

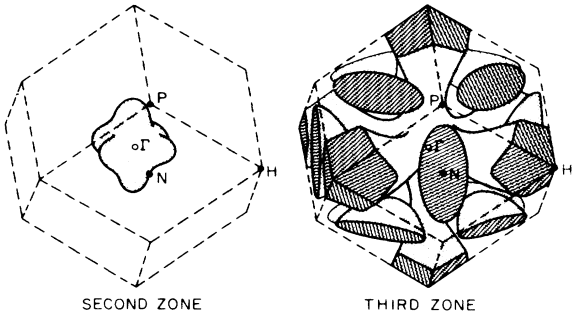

FIG. 2. (a) Γ-centered hole octahedron; (b) N-centered ellipsoids and the JG surface [after Mattheis (Ref. 17)].

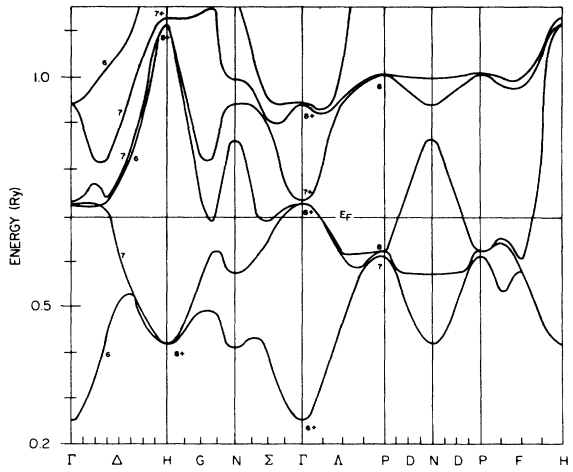

FIG. 3. The band-structure of Nb as calculated by Elyashar and Koelling (Ref. 23).

have been presented earlier in the work of Karim *et al.*,[8] we will limit ourselves here to a discussion of those quantities used as input for the Fermi-surface deconvolution programs. In addition, a discussion will be given of some experimental data, taken in the earlier investigation, which can be better understood with the availability of the detailed parametrization of the surface achieved here. We refer the reader to the paper of Karim *et al.*[8] for a review of the earlier experimental work of Halloran *et al.*[15] and Scott and Springford.[16] Band-structure calculations have been performed by Mattheiss,[17] Boyer *et al.*,[18] Deegan and Twose,[19] Euwema,[20] and Anderson *et al.*[21] Fully relativistic calculations employing a general non-muffin-tin potential (nonspherical, nonflat) with an $\alpha=\frac{2}{3}$ exchange correlation potential were carried out by Elyashar and Koelling;[22,23] our experimental work was initiated in parallel with this latter theoretical work. Calculations using the pseudopotential approach were made by Ho, Louie, Chelikowsky, and Cohen.[24]

Figures 1 and 2 (due to Mattheiss[17]) show the bcc Brillouin zone and Fermi surface of Nb. The band structure as calculated by Elyashar and Koelling is shown in Fig. 3. The surface contains a closed "octahedron" (OCT) hole sheet in the second zone, and two sheets in the third zone: the "ellipsoids" (ELL) which are centered on the N points of the zone, and the "jungle gym" (JG) which is topologically equivalent to a set of cylinders extending in the ⟨100⟩ directions and which intersect at the Γ and H points of the zone.

A. Fermi radii

dHvA areas which are extremal with respect to orientation are least sensitive to sample misalignment and only such data were used as input to our programs. In addition, *in situ* NMR calibration of the magnet assured high absolute accuracy of the data. The following cross sections were employed in the fit: the Γ-centered (100), (111), and (110) orbits on the hole octahedron, the (100) N-centered electron orbit on the JG, the Γ- and H-centered (111) JG intersections, the (100) and the two nonsymmetry related principal (110) N-centered ellipsoidal orbits, and the (100) JG arm. For a detailed description of the topology of these orbits we refer to the work of Karim *et al.*[8]

Table I lists the ten orbits employed in the fit, the experimental and fitted areas, and the percentage error in the fit. The overall rms error of the fit is 0.31%. Our data was weighted so that the quantity

$$\Delta^2=\frac{1}{N}\sum_{i=1}^{N}\left[\frac{A_i^{(\mathrm{calc})}-A_i^{(\mathrm{expt})}}{A_i^{(\mathrm{expt})}}\right]^2$$

was a minimum, i.e., $W_i=1$ in Eq. (10).

Table II gives a set of values of the quantities $\partial A_i/\partial\eta_l$. These quantities are important in converting Dingle temperature data to obtain point scattering lifetimes as discussed by Coleridge.[25] They also indicate the sensitivity of a given area to a change in a specific phase shift. They are more sensitive to the grid size used in tracing the orbit than are the areas themselves. The phase shifts themselves resulting from the procedures of Sec. II are contained in Table III.

With the phase shifts we may calculate the Fermi radius of any point on the Fermi surface. The radii of the second zone surface in a plane passing through Γ normal to the ⟨100⟩ and ⟨110⟩ directions are shown in Fig. 4. Shown also are the corresponding radii calculated by Koelling[14] using the fully non-muffin-tin (nonspherical,

TABLE I. Experimental and fitted extremal cross-sectional areas in Nb. See Ref. 8 for orbit name conventions.

Orbit	Experimental area (a.u.)	Fitted area (a.u.)	Error
OCT Γ $\gamma_1\langle 100\rangle$	0.2798	0.2796	0.57%
OCT Γ $\gamma_1\langle 111\rangle$	0.1351	0.1351	0.01%
OCT Γ $\gamma_1\langle 110\rangle$	0.2092	0.2096	0.19%
JG N $\Delta\langle 100\rangle$	0.4053	0.4047	0.16%
JG Γ $\gamma_2\langle 111\rangle$	0.2319	0.2315	0.16%
JG H $\eta\langle 111\rangle$	0.5192	0.5230	0.74%
ELL N $\nu_{1,2}\langle 100\rangle$	0.1790	0.1791	0.06%
ELL N $\nu_1\langle 110\rangle$	0.2131	0.2134	0.13%
ELL N $\nu_2\langle 110\rangle$	0.2409	0.2406	0.13%
JG $\alpha\langle 100\rangle$	0.03873	0.03868	0.14%

TABLE II. Phase-shift derivatives of extremal cross-sectional areas. Areas are in Brillouin units, phase shifts in radians, and energies in $2\pi/a$ units.

Orbit	$\frac{\partial A}{\partial \eta_s}$	$\frac{\partial A}{\partial \eta_p}$	$\frac{\partial A}{\partial \eta_{d(e_g)}}$	$\frac{\partial A}{\partial \eta_{d(t_{2g})}}$	$\frac{\partial A}{\partial \eta_f}$	$\frac{1}{\pi}\left[\frac{\partial A}{\partial E}\right]_\eta$
OCT Γ $\gamma_1\langle 100\rangle$	$-0.429\,00\times10^{-2}$	$-0.137\,79$	$-0.160\,21$	$-0.736\,89$	-4.8785	$-0.260\,00$
OCT Γ $\gamma_1\langle 111\rangle$	$-0.760\,00\times10^{-3}$	$-0.204\,90\times10^{-1}$	$-0.368\,00\times10^{-2}$	$-0.723\,99$	-1.5863	$-0.140\,00$
OCT Γ $\gamma_1\langle 110\rangle$	$-0.234\,00\times10^{-2}$	$-0.101\,15$	$-0.882\,30\times10^{-1}$	$-0.702\,49$	-3.4543	$-0.210\,00$
JG N $\Delta\langle 100\rangle$	0.3376×10^{-1}	$0.518\,82$	$0.101\,42$	$0.670\,12$	5.8994	0.4000
JG Γ $\gamma_2\langle 111\rangle$	$-0.483\,80\times10^{-1}$	$-0.579\,08$	$-0.137\,32$	$-0.885\,09$	-6.6003	$-0.480\,00$
JG H $\eta\langle 111\rangle$	-0.8648×10^{-1}	$-0.312\,12$	$-0.307\,80\times10^{-1}$	$-0.472\,18$	-4.7876	$-0.310\,00$
ELL N $\nu_{12}\langle 100\rangle$	$-0.147\,57$	-1.3232	$-0.163\,38$	-0.7586×10^{-1}	-3.0343	$-0.680\,00$
ELL N $\nu_1\langle 100\rangle$	0.0000	-1.5539	$-0.104\,80$	$-0.953\,80\times10^{-1}$	-1.1565	$-0.650\,00$
ELL N $\nu_2\langle 110\rangle$	$-0.164\,01$	-1.6561	$-0.497\,70\times10^{-1}$	$-0.170\,56$	-2.1400	$-0.790\,00$
JG $\alpha\langle 100\rangle$	$-0.977\,21\times10^{-2}$	$-0.135\,75$	$-0.294\,79\times10^{-1}$	$-0.249\,10$	-1.8041	$-0.120\,00$

TABLE III. Phase shifts η and their energy derivatives η' derived from the KKR fitting procedure.

	s	p	$d(e_g)$	$d(t_{2g})$	f
η	$-0.896\,02$	2.7634	-2.1881	-2.0519	$0.004\,326\,7$
η'	4.2002	$-0.176\,66$	18.130	16.391	$-0.171\,39$
	$E_F=0.695$ [$(2\pi/a)^2$ units]			lattice constant $=6.2286$ (Bohr radii)	

TABLE IV. Surface averaged properties in Nb for each of the three sheets of the Fermi surface. The band density of states is from the empirically adjusted calculation of Koelling (Ref. 14).

	Ellipsoids (total of six)	Octahedron	JG	Total
Number of carriers per atom (KKR fit)	-0.4118	-0.06919	-0.5224	-1.003
Enhanced density of states (KKR fit) states/eV atom	1.249	0.547	1.573	3.360[a]
Band density of states (APW calculation[b]) states/eV atom	0.596	0.202	0.648	1.446
$\langle\lambda\rangle_{\text{sheet}}$	1.10	1.71	1.43	1.33
$\langle\Delta\rangle_{\text{sheet}}/\Delta_0$	0.9	1.0	1.1	

[a]Heat-capacity value of Ref. 26 is 3.320.
[b]From Ref. 14.

TABLE V. Derivatives of the volumes of the three sheets of the Fermi surface of Nb with respect to energy and phase shifts. Volumes are in Brillouin units, energies in $2\pi/a$ units, and phase shifts in radians.

Sheet	$\frac{\partial V}{\partial \eta_s}$	$\frac{\partial V}{\partial \eta_p}$	$\frac{\partial V}{\partial \eta_d(e_g)}$	$\frac{\partial V}{\partial \eta_d(t_{2g})}$	$\frac{\partial V}{\partial \eta_f}$	$\left.\frac{\partial V}{\partial E}\right\|_\eta$
ELL	$-0.052\,80$	-0.7684	$-0.052\,61$	$-0.053\,32$	-0.9824	-1.1345
JG	$-0.080\,00$	-0.9257	-0.1147	-1.153	-9.153	-2.181
OCT	$-0.001\,223$	$-0.062\,62$	$-0.039\,27$	-0.4162	-1.947	-0.3762

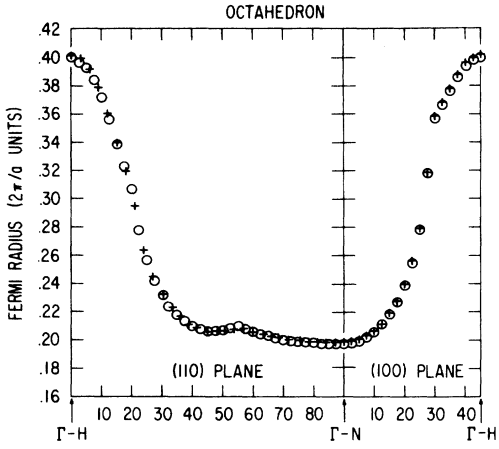

FIG. 4. The parametrized radii of the second-zone octahedron in a plane passing through Γ and normal to the ⟨110⟩ and ⟨100⟩ directions (○). Shown also are the corresponding Fermi radii as calculated by Koelling (Ref. 14) (+).

nonflat) self-consistent, relativistic augmented-plane-wave programs of Elyashar and Koelling[23] with $\alpha=\frac{2}{3}$ used for the exchange correlation contribution to the potential. This calculation was empirically adjusted in that the p-wave logarithmic derivative was shifted downward by 0.05 Ry and the Fermi energy recalculated; this correction shifts the results in the direction of the pseudopotential calculations of Ho *et al.*[24]

The radii of the third-zone JG surface in planes passing through Γ and perpendicular to (100) (Γ*NH* plane) and (110) (Γ*NP* plane) are shown in Fig. 5; we again show the corresponding radii of Koelling. Finally, the inverted and calculated radii in the *NΓH*, *NHP*, and *NΓP* planes for the *N*-centered ellipsoid are shown in Fig. 6. The relationships of all the symmetry-plane Fermi radii to the Brillouin zone boundaries is given by the "house plot" shown in Fig. 7.

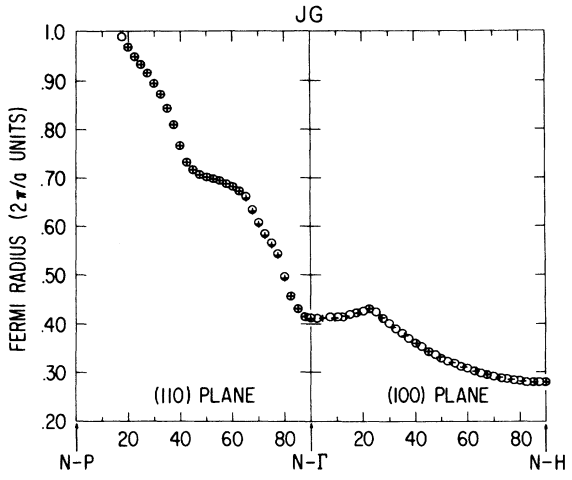

FIG. 5. The parametrized radii (○) of the third-zone JG surface in planes passing through Γ normal to (110) (the Γ*NP* plane) and (100) (the Γ*NH* plane) and the calculated values of Koelling (Ref. 14) (+).

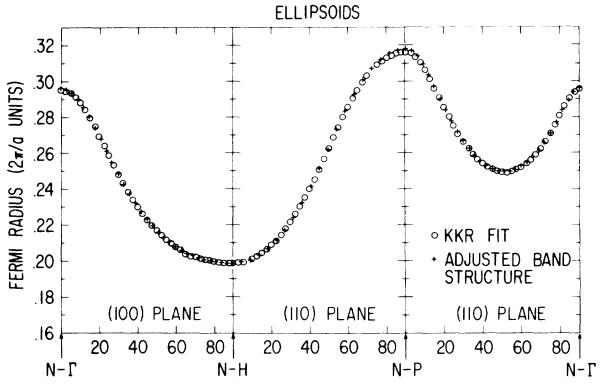

FIG. 6. The parametrized radii of the *N*-centered ellipsoid (○) in the *NΓH*, *NHP*, and *NΓP* planes, and the radii of Koelling (Ref. 14) (+).

The numbers of carriers in each of the three independent sheets of the Nb surface were computed using the techniques described in Appendix B. These are listed in Table IV; note that the sum is −1.003, within 0.3% of that required by the charge neutrality condition for this odd valent metal. The values of $\partial V/\partial\eta_l$, the phase-shift derivatives of the volume, are given for each sheet in Table V.

B. Interpretation of κ, α', and α''.

In this section we apply the parametrization scheme to the interpretation of several unexplained features in the Fermi-surface experiments on Nb. Figure 8 shows the ellipsoid and octahedron areas observed in the two symmetry planes by Karim *et al.*[8] The branch labeled κ at about

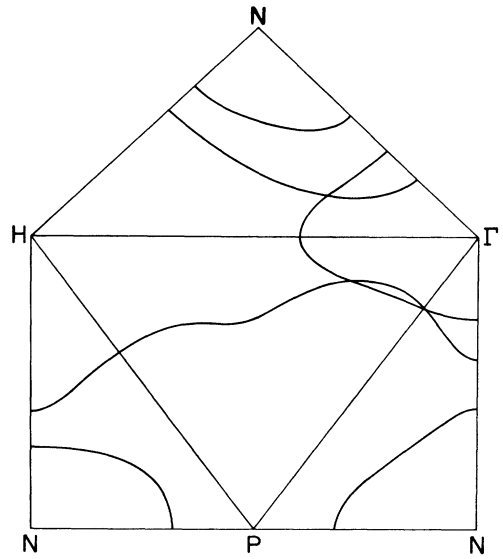

FIG. 7. "House plot" showing contours of the parametrized Fermi surface in the (100) and (110) symmetry planes relative to the Brillouin zone.

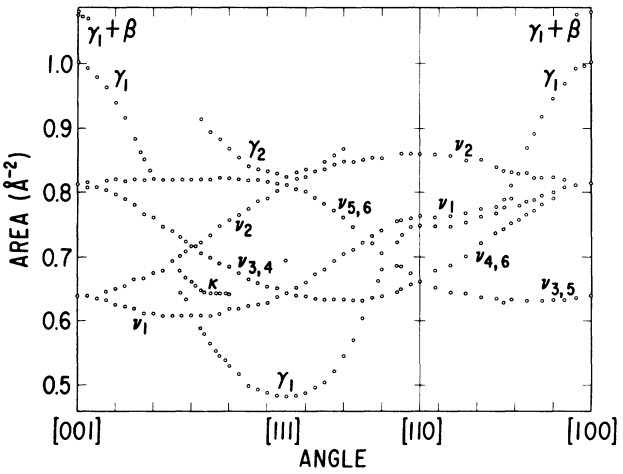

FIG. 8. Observed cross-sectional areas for the ellipsoid and octahedron surfaces [from Karim *et al.* (Ref. 8)]. The κ orbit is shown in the text to be a noncentral orbit on the octahedron.

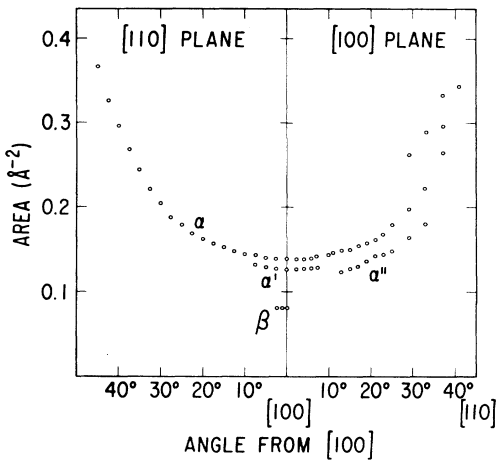

FIG. 9. Observed cross-sectional areas for the α, α', α'', and β orbits [from Karim *et al.* (Ref. 8)]. α is a noncentral orbit around the JG arm. β has previously been shown (Ref. 8) to be a quantum-interference orbit. α' and α'' are argued in the text to be noncentral breakdown orbits between the JG and the octahedron.

30° from ⟨001⟩ in the (110) plane cannot be explained by symmetry centered orbits on either of these sheets. We have previously suggested[8] that κ may be due to noncentral orbits on either the octahedron or the JG. As described below, the parametrization scheme confirms that such a noncentral orbit exists on the octahedron.

We searched for noncentral orbits by choosing a field direction, tracing several orbits at successively larger displacements of the orbit center from Γ along the field direction, and looking for an extremal area. For the field greater than about 26° from ⟨001⟩ in the (110) plane, a noncentral maximal orbit on the octahedron appears. We followed this noncentral orbit in the parametrization as far as 54.7° from ⟨001⟩, where the search was terminated. Physically we expect the orbit to continue for larger angles and eventually rejoin the central orbit. Experimentally the orbit is seen over a more limited range, perhaps because the mass or the curvature factor becomes unfavorable. Table VI shows the measured and calculated areas and the displacement of the orbit center from Γ for five field directions. The agreement of the areas predicted by the parametrization with those experimentally measured for the κ orbit is excellent, within 2% for all angles.

Another unexplained feature of the Fermi surface is the origin of the α' and α'' branches for angles near ⟨100⟩ as shown in Fig. 9. These orbits have been seen and discussed in all the experimental studies[8,15,16] of Nb. The α branch is well understood as a set of minimum-area noncentral orbits on the JG arm centered on the Γ-H line. The α' and α'' orbits have been attributed to noncentral orbits on the protrusion of the octahedron in the ⟨100⟩ direction,[16] and to magnetic breakdown between the octahedron and the JG.[8] The parametrization scheme shows the latter possibility is most probably correct.

Consider first the α' orbit at ⟨100⟩. The relative positions of the octahedron and JG are shown in Fig. 7. In our nonrelativistic description of the surface these two sheets touch at three points in the irreducible $\frac{1}{48}$th of the zone: once in the ΓHN plane and twice in the ΓHP plane. Spin-orbit effects lift these degeneracies and create a small gap in **k** space across which magnetic breakdown may occur. We have examined orbits on the octahedron and JG for the field along the Γ-H line which pass close to the breakdown point in the ΓHN plane. Figure 10 shows the geometry typical of the two orbits for centers farther from Γ than the breakdown point. In addition to orbits on the JG and octahedron, there are three possible breakdown orbits whose areas differ by the crosshatched area δ: JG-δ, JG-2δ, JG-3δ. The areas of these orbits were calculated in the parametrization using a Simpson's rule integration of the δ area assuming the breakdown orbit switches suddenly at the angle of closest approach from

TABLE VI. Calculated orbit centers and areas for noncentral orbits on the octahedron corresponding to the experimentally observed κ branch. Areas and lengths are in Brillouin units. Orbit center refers to displacement from Γ along the field direction.

Angle from ⟨001⟩ in (110) plane	Orbit center (bu)	Calc. area (bu)	Expt. area (bu)	Difference
27°	0.033	0.1857	0.1888	1.64%
30°	0.066	0.1794	0.1816	1.21%
35°	0.093	0.1758	0.1771	0.73%
45°	0.120	0.1752		
54.7°	0.136	0.1783		

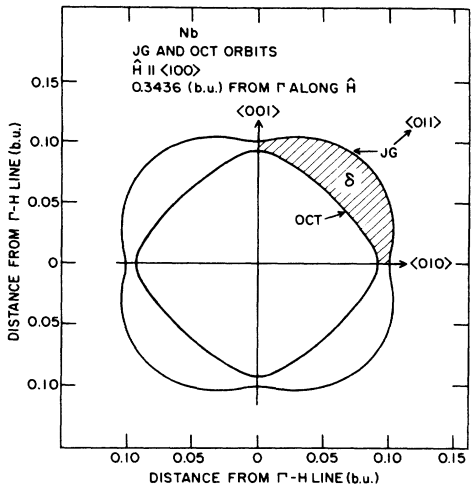

FIG. 10. JG and octahedron (OCT) orbits for the field along ⟨100⟩, with orbit center displaced 0.3436 bu from Γ. If breakdown occurs at the angle of closest approach, orbits corresponding to JG-δ, JG-2δ, and JG-3δ appear.

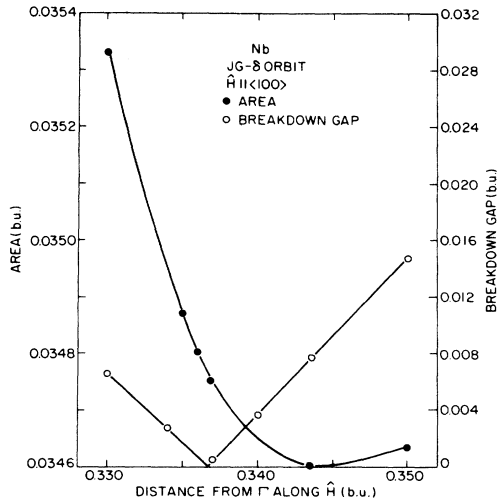

FIG. 11. Variation of area and breakdown gap with displacement of orbit center from Γ for the JG-δ orbit, for the field in the ⟨100⟩ direction.

one surface to the other. As the position of the orbit centers was varied, a minimum was found in the JG orbit area at 0.3359 Brillouin unit (bu) (see Appendix A for a discussion of units) from Γ corresponding to the observed α orbit. The JG-δ orbit also displayed a minimum, at 0.3436 bu from Γ, whose area is within 1% of the measured α' area. The JG-2δ, JG-3δ, and OCT orbits do not have extrema for any position of the orbit center. Thus we interpret the α' orbit as a noncentral breakdown orbit between the JG and the octahedron involving the near degeneracy of the two sheets in the Γ*HN* plane. The earlier suggestion that α' is a noncentral orbit on the octahedron is not supported by the parametrization.

Given this interpretation of the α' orbit, an interesting question arises as to the condition determining the orbit center. Normally the amplitude of quantum oscillations due to a particular cyclotron orbit is a slowly varying function of the position of the orbit center along the field direction. This allows destructive interference between oscillations due to neighboring orbits to eliminate all oscillations except those whose frequency ($\propto$ orbital area) is extremal. For a noncentral breakdown orbit like JG-δ the amplitude of the oscillations is not a slowly varying function of the position of the orbit center. The oscillation amplitude depends strongly on the breakdown probability and therefore decreases rapidly as the orbit center is moved away from the position where the breakdown gap is smallest. This strong amplitude dependence effectively eliminates the orbits not centered close to the minimum gap position and they cannot contribute to the destructive interference needed to give the extremal area condition. If the amplitude dependence is very strong, the extremal area condition may be irrelevant, the "orbit center" being determined by the position where breakdown is most probable. For this to be the case the amplitude would have to lose most of its magnitude in a distance comparable to that over which the argument of the oscillating term changes by 2π. For breakdown orbits centered on a symmetry point, the extremal area condition and the maximum breakdown probability condition are satisfied simultaneously and there is no competition between them.

For the JG-δ orbit, the position of minimum area and the position of minimum breakdown gap do not coincide, as illustrated in Fig. 11. (Because our parametrization is not relativistic, we find the breakdown gap going to zero rather than to a minimum as would be the case if spin-

TABLE VII. Orbit centers and areas for the JG-δ and JG-2δ orbits. The orbit centers were fixed by the condition that the area be extremal. Orbit center column refers to distance of the orbit center from Γ, along the field direction. Areas and lengths are in Brillouin units. NF means not found in the parametrization.

	JG-δ		α'	JG-2δ		α''
Angle from ⟨001⟩ in (100) plane	Orbit center (bu)	Area (bu)	Area (bu)	Orbit center (bu)	area (bu)	area (bu)
0°	0.3436	0.0346	0.0344	NF	NF	
3°	0.3425	0.0351	0.0349	NF	NF	
7°	0.3390	0.0359	0.0353	0.3415	0.0312	
15°	NF	NF		0.3270	0.0350	0.0346

orbit effects were taken into account.) The two conditions give orbit centers which are about 2% different in their displacement from Γ and areas differing by less than 0.5%. This area difference is within experimental error, so the measured area cannot be used to determine whether the extremal area condition or the minimum breakdown-gap condition is most important. However, if the minimum breakdown-gap condition were dominant, we would expect to observe orbits with areas JG-2δ and JG-3δ, since the breakdown probability for these orbits is the same as for JG-δ if the field is along ⟨100⟩. The absence of these orbits suggests that the extremal area condition is dominant, though the orbit center may be shifted somewhat toward the minimum gap position. The areas and orbit centers for the JG-δ orbit as a function of angle for the field in the (100) plane assuming the extremal area condition are shown in Table VII.

The disappearance of the α' branch and the appearance of the α'' branch as the field is tipped off ⟨100⟩ can be explained by our interpretation. As the field is tipped in the (100) plane two of the breakdown gaps on opposite sides of the orbits in Fig. 10 remain fixed, while the other two move closer and farther from Γ, respectively. This is illustrated in Fig. 12, for an angle of 7° from ⟨100⟩. This means that the two breakdowns required for the JG-δ orbit can no longer both be close to the minimum gap position. At some angle the gap at one of the junctions becomes so large that the orbit fails to complete, explaining the disappearance of the α' branch.

We interpret the α'' branch as an orbit of the form JG-2δ. Tipping the field does not adversely affect this orbit, because the two breakdowns required are on opposite sides of the orbit and can be simultaneously brought as close as desired to the minimum gap value by adjusting the position of the orbit center. Table VII shows that for angles greater than 7° from ⟨100⟩ a minimum occurs in the JG-2δ orbit as a function of orbit-center position. This accounts for the appearance of α'' at angles away from ⟨100⟩. The dHvA experiments do not observe the α'' orbit for angles less than 13° from ⟨100⟩, possibly because the breakdown probability in this region is too low. At 15° from ⟨100⟩ the predicted area of JG-2δ agrees to within 1.5% with the measured area of α''. At this angle the positions of minimum area and minimum breakdown gap are nearly identical, as shown in Fig. 13.

The absence of α'' oscillations in the (110) plane is consistent with its being a breakdown orbit of the form JG-2δ. For the field in the (110) plane the symmetrically equivalent breakdown points are adjacent rather than on opposite sides of the orbits as is the case in the (100) plane. Therefore it is impossible to find an orbit center where the two gaps involved in the JG-2δ orbit are simultaneously small. Our interpretation also allows for the unusual angular dependence of the dHvA amplitudes of the α' and α'' orbits seen in the experiments.[15,16] These amplitudes depend strongly on the breakdown probability, which may vary considerably with field direction as the positions of extremal area and minimum gap move relative to each other.

In summary, we have argued that the κ, α', and α'' orbits may be interpreted via the parametrization scheme as noncentral orbits due to local deformations of the Fermi surface. We have previously interpreted the β orbit using an earlier parametrization as a quantum interference orbit.[8] We have thus interpreted all of the unexplained features in the Fermi measurements of Nb, and get excellent quantitative agreement between experiment and parametrization. The fact that the parametrization can accurately predict the fine details of the Fermi surface geometry responsible for these noncentral breakdown orbits, with only five parameters fitted to only symmetry direction areas, demonstrates explicitly how powerful and useful the KKR schemes can be.

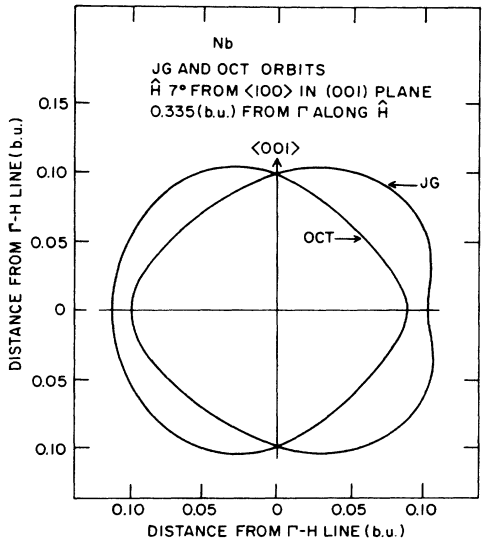

FIG. 12. JG and octahedron orbits for the field tipped 7° from ⟨100⟩ in the (110) plane. The orbit center is 0.335 bu from Γ along the field direction.

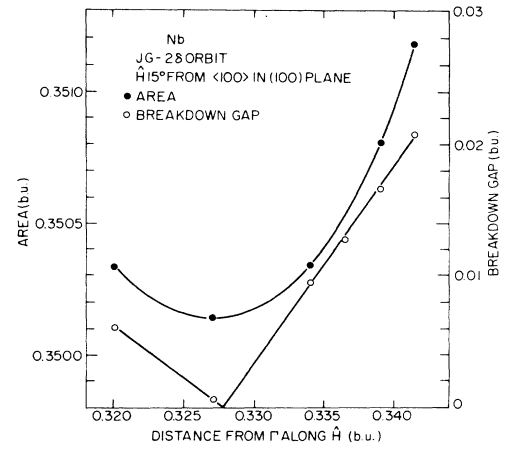

FIG. 13. Variation of area and breakdown gap with displacement of orbit center from Γ along the field direction for the JG-2δ orbit, for the field 15° from ⟨100⟩ in the (100) plane.

TABLE VIII. Experimental and fitted cyclotron effective masses for symmetry direction orbits in Nb (entries with a negative sign correspond to hole orbits).

Orbit	Expt. Mass	Fitted Mass	Error
OCT Γ $\gamma_1\langle 100\rangle$	−4.9	−4.76	2.9%
OCT Γ $\gamma_1\langle 111\rangle$	−3.75	−3.86	2.9%
OCT Γ $\gamma_1\langle 110\rangle$		−4.20	
JG N $\Delta\langle 100\rangle$	4.28	4.18	2.4%
JG Γ $\gamma_2\langle 111\rangle$		−5.57	
JG H $\eta\langle 111\rangle$	−2.69	−2.79	3.8%
JG $\alpha\langle 100\rangle$	−1.53	−1.50	2.1%
ELL N $\nu_{12}\langle 100\rangle$	−1.94	−1.97	1.6%
ELL N $\nu_1\langle 110\rangle$	−1.58	−1.60	1.2%
ELL N $\nu_2\langle 110\rangle$	−2.03	−1.98	2.6%

C. Fermi velocities

We now discuss our parametrization of the effective masses through the energy derivatives of the phase shifts using Eq. (13). The required parameters $\partial A_i/\partial\eta_l$ and $\partial A_i/\partial E$ are to be found in Table II. Table VIII lists the experimental and fitted values of the effective masses for the eight orbits employed in the fit. The resulting rms error of 2.5% is quite satisfactory given the accuracy of effective mass data. At this point we note that by the above procedure we implicitly assume that all many-body effects can be absorbed in the η_l', which, in the theory, are intended to describe only the one-electron behavior. Empirically, the good quality of fit suggests that this is a reasonable procedure. Furthermore, it is well known that phase-shift parametrizations of Fermi surfaces are quite insensitive to the chosen value of the Fermi energy parameter. Therefore, we could equally well have fit our masses by suppressing the structure constant term, $(\partial A/\partial E)_{\eta_l}$, entering Eq. (13). In this case a uniform mass enhancement, a commonly employed assumption, can be incorporated in the scheme simply by uniformly rescaling the η'. The anisotropy in the many-body enhancement of the Fermi velocities as derived below is much smaller than that found in the bare band velocities (see Fig. 14). Thus it is reasonable to expect that the many-body effects in the velocities can be described by a small readjustment of the η' about a uniform rescaling.

With the availability of the η_l and η_l', we can generate the Fermi velocity at any point on the surface using Eqs. (3)—(7). Figure 14 shows, for all three sheets, the absolute values of the Fermi velocity deduced from the fit, together with the band-structure values of Koelling,[14] and the derived enhancement factor defined by Eq. (1). The dashed lines on the ellipsoid curves are smooth interpolations through regions of free-electron singularities (defined as points, or more precisely, lines, where the free-electron sphere for the chosen value of the Fermi-energy parameter intersects the parametrized surface). At such points the KKR formalism is singular and in the neighboring region the convergence of the structure factor sums is slow, resulting in a loss in accuracy. The sharp bumps in the curves for the octahedron and JG are artifacts of the fitting procedure where the two sheets touch (or intersect) in the nonrelativistic approximation, resulting in a discontinuity in the velocity.

With the availability of both Fermi velocities and radii, we can calculate the density of states for each sheet using Eqs. (B2) or (B4). The density of states for each sheet for the fitted surface and the APW calculations of Koelling are listed in Table IV. The total electronic density of states for Nb summed over the three sheets is 3.360 states/eV atom which we refer to as the quasiparticle density of states; this is to be compared with the thermal density of states extracted from heat capacity measurements of 3.320,[26] in agreement to within 1.2%. The equality of the density of states as determined by these two methods is expected from modern many-body theory.

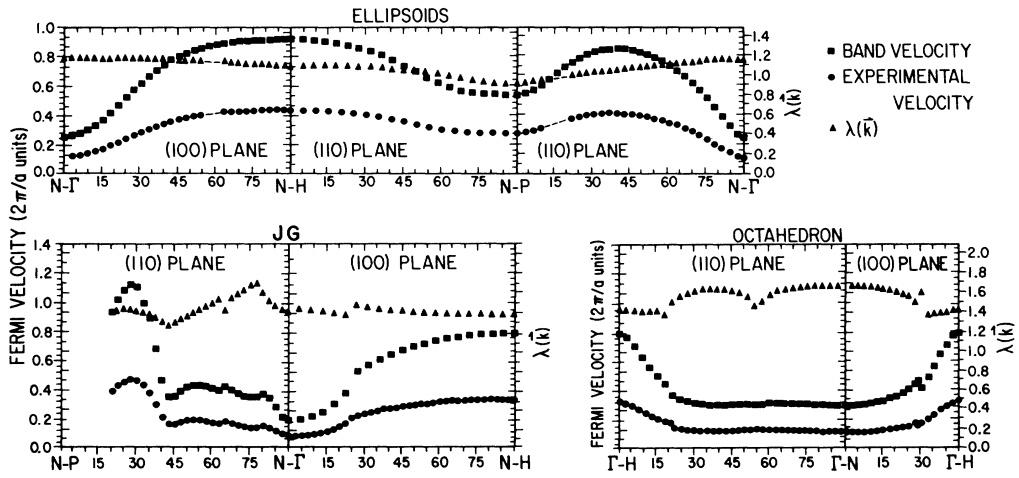

FIG. 14. Fermi velocities derived from the parametrization of experimental masses and from the empirically adjusted band calculation of Koelling (Ref. 14) for the three sheets of the Nb Fermi surface (left-hand scale). The derived values of $\lambda(\mathbf{k}) = |\mathbf{v}(\mathbf{k})_{\text{band}}/\mathbf{v}(\mathbf{k})_{\text{expt}}| - 1$ are also shown (right-hand scale).

IV. THE ANISOTROPIC MANY-BODY ENHANCEMENT

In addition to $|\mathbf{v}(\mathbf{k})|$, Fig. 14 also contains the dimensionless many-body-enhancement factor $\lambda(\mathbf{k})$ defined by Eq. (1); the magnitude is displayed on the scale at the right. We note that this quantity is clearly anisotropic. The anisotropy in $\lambda(\mathbf{k})$ takes a particularly simple form which simplifies comparison with theory. Within any given sheet, the values of λ shown in Fig. 14 do not deviate by more than about 10% from the average value for that sheet. In contrast, the average values show considerable variation from sheet to sheet. This means that most of the anisotropy is very well described by the average values for each of the sheets, the variation within any sheet being much less important. These three average values were derived by using the densities of states from each sheet as obtained in the KKR fit and the band structure in the expression

$$\frac{\langle N_{\mathrm{KKR}}\rangle_{\mathrm{sheet}}}{\langle N_{\mathrm{band}}\rangle_{\mathrm{sheet}}}=1+\langle\lambda\rangle_{\mathrm{sheet}}\ .$$

This is equivalent to averaging $\lambda(\mathbf{k})$ with a weighting factor $1/|\mathbf{v}_{\mathrm{band}}(\mathbf{k})|$:

$$\langle\lambda\rangle_{\mathrm{sheet}}=\frac{\int_{\mathrm{sheet}}[\lambda(\mathbf{k})/|\mathbf{v}_{\mathrm{band}}(\mathbf{k})|]dS}{\int_{\mathrm{sheet}}[1/|\mathbf{v}_{\mathrm{band}}(\mathbf{k})|]dS}\ .$$

These sheet average values are shown in Table IV.

Three approaches to calculating the electron-phonon renormalization of the Fermi velocity in Nb have been explored. The most popular approach uses the so-called rigid-muffin-tin approximation,[27,28] where the nucleus and surrounding charge contained inside the muffin-tin radius are assumed to move rigidly during a lattice distortion. This assumption allows the calculation to make use of several quantities directly calculated by band theory and has been shown to give reasonable results for many elements. However, the approximation is unphysical in that no allowance is made for deformation of the charge cloud surrounding the nucleus when it moves off its equilibrium position, an effect that is likely to modify the interatomic forces.

The second approach is the tight-binding[12] scheme, where the band energies are calculated with linear combination of atomic orbitals (LCAO) methods which contain the nuclear position as an explicit parameter. The dependence of the band energies on the atomic displacement allows the effective interatomic potential to be obtained without the rigid-muffin-tin assumption. The tight-binding scheme is particularly appropriate for transition metals because the *d* electrons which dominate many of the electronic properties are described by the LCAO scheme much better than are the more extended *sp* electrons in simple metals.

A further improvement[13,29] on the tight-binding scheme is made by explicitly allowing the Bloch states constructed from atomic orbitals to be nonorthogonal. This flexibility for the electronic wave functions is especially important for calculating electron-phonon effects because Bloch states which are orthogonal when the atoms occupy their equilibrium positions become nonorthogonal when the atoms are displaced.

Comparison of the anisotropy in λ for these three methods with the experimental results reported here provides the opportunity to test the ability of theory to describe the electron-phonon effects for individual $\mathbf{k}$ states. We take for comparison the three values of $\lambda_{\langle\mathrm{sheet}\rangle}$ on the ellipsoids, octahedron, and JG because these summarize the experimental results very well and can be calculated in the theories more easily than can the point values $\lambda(\mathbf{k})$. Table IX makes this comparison, showing the sheet values and overall surface averages.

Table IX shows two important features. First, there is a great deal of variation in the calculated values for the Fermi-surface average of λ. This is not unexpected, because λ is proportional to the magnitude of the electron-phonon coupling constant, a quantity which must be set outside the calculation and for which there is no generally accepted value. The calculated average value of λ is not related to whether the calculation was done by the rigid-muffin-tin or tight-binding method. Both methods produced one low and one high value, with the average of the two results by each method very close to 1.33, the result of our work.

The second noteworthy feature of Table IX is the anisotropy in the values of λ for the three sheets of the Fermi surface. This anisotropy is more clearly examined in the normalized values of λ shown in parentheses, where the

TABLE IX. Comparison of anisotropy in the electron-phonon enhancement factor λ derived from calculations using the rigid-muffin-tin (RMT) approximation, the orthogonal tight-binding (OTB) scheme, and the nonorthogonal tight-binding (NTB) scheme with values derived in this work. The numbers in parenthesis are normalized so that the surface average value is 1.00.

Method used	Ellipsoids	Octahedron	JG	Total
RMT from Ref. 10	1.85	1.28	1.37	1.58
	(1.17)	(0.810)	(0.867)	(1.00)
RMT from Ref. 11	1.17	1.09	1.08	1.12
	(1.04)	(0.973)	(0.964)	(1.00)
OTB from Ref. 12	1.35	1.92	1.90	1.69
	(0.799)	(1.14)	(1.12)	(1.00)
NTB from Ref. 13	0.80	1.10	1.14	0.99
	(0.81)	(1.11)	(1.15)	(1.00)
This work	1.10	1.71	1.43	1.33
	(0.827)	(1.29)	(1.07)	(1.00)

normalization has been chosen to make the surface average value equal to 1.00. Our results show that the octahedron has the largest electron-phonon coupling, the ellipsoids the smallest coupling, and the JG intermediate coupling. The range of anisotropy is 46% between the octahedron and ellipsoids. None of the calculations produces such a wide range, the anisotropies being $\sim 35\%$ in three of them and only 8% in the fourth. There is a systematic difference between the rigid-muffin-tin and tight-binding calculations with respect to the trends in the anisotropy: the rigid-muffin-tin calculations have the ellipsoids with the largest coupling, while the tight-binding calculations and our results have the ellipsoids with the smallest coupling. The tight-binding results both have the octahedron and JG approximately equal in coupling, while our results show a 22% difference between these two sheets. The average value of the coupling on the octahedron and JG in both tight-binding calculations is in reasonable agreement with the average value for these two sheets in our results. We conclude that the tight-binding methods predict the anisotropy in λ much better than do the rigid-muffin-tin methods, although neither method correctly distinguishes the anisotropy between the octahedron and the JG.

Empirically there is a correlation between the anisotropy of λ and the anisotropy of the Fermi velocity as given in either the band calculation or in our results. Table IX and Fig. 14 show that λ is large where v_F is small and vice versa. The size of v_F is, in turn, correlated with the fraction of d character in the electronic wave function: The larger the d character, the smaller v_F. The Fermi velocities and amount of d character are considerably different between the ellipsoids and either the JG and the octahedron; the differences between the JG and octahedron are much smaller. These observations suggest two conclusions: (1) the amount of d character in the wave function is one factor which controls the strength of the electron-phonon coupling, and (2) the tight-binding calculations are more successful than the rigid-muffin-tin calculations in predicting the anisotropy of λ because they are able to distinguish the difference between the deformations of the d and sp charge densities when an atom moves off its equilibrium position. Apparently, the tight-binding calculations are not sensitive to the difference in d character between the octahedron and JG. It is possible that the difference in electron-phonon coupling between these two sheets depends on more subtle features like the relative amount of e_g and t_{2g} character or the directional character in the electronic wave function of the relevant phonon displacements. The addition of nonorthogonality does not seem to be a crucial improvement in describing the electron-phonon anisotropy in Nb.

V. GAP ANISOTROPY

Our results for the anisotropy in $\lambda(\mathbf{k})$ can be used to infer the anisotropy in the superconducting energy gap $\Delta(\mathbf{k})$. The connection between $\lambda(\mathbf{k})$ and $\Delta(\mathbf{k})$ can be obtained with the same methods used to derive the empirical T_c formulas of McMillan,[30] and Allen and Dynes.[31] In those derivations λ and μ^* are assumed to be $\mathbf{k}$ independent. If λ and μ^* are allowed to be weakly anisotropic, the equations can be expanded about the average values of λ and μ^* keeping no terms higher than linear in $[\lambda(\mathbf{k})-\lambda]$ and $[\mu^*(\mathbf{k})-\mu^*]$. This gives the expression

$$\frac{\Delta(\mathbf{k})}{\Delta_0}=1+\frac{1+\mu^*}{(1+\lambda)(\lambda-\mu^*)}[\lambda(\mathbf{k})-\lambda] - \frac{1}{\lambda-\mu^*}[\mu^*(\mathbf{k})-\mu^*] , \tag{15}$$

which was first derived by Butler and Allen[32] in terms of Fermi-surface harmonics, and later by Allen[33] and Askenazi, Dacarogna, and Allen.[34] Δ_0 is the value of the gap averaged over the entire surface. At present there is no experimental knowledge of the anisotropy in $\mu^*(k)$, but calculations[12,34] suggest that the second term in Eq. (15) contributes about 30% to the gap anisotropy while the first term contributes 70%. If we ignore the second term, our data for $\lambda(\mathbf{k})$ gives a direct estimate of the variation in $\Delta(\mathbf{k})$ over the Fermi surface. It is important to note that a general direction in $\mathbf{k}$ space may intersect as many as three sheets of the Fermi surface, so that three gaps may exist simultaneously. Because the values of $\lambda(\mathbf{k})$ are grouped close to the average values for the three sheets, the values of $\Delta(\mathbf{k})$ will follow a similar pattern. The average values of $\Delta(\mathbf{k})$ for each sheet are shown in Table IV.

There has been considerable speculation in the literature on the possibility of multiple gaps[35] in Nb suggested by specific heat,[36] ultrasonic attenuation,[35] and tunneling data.[37] These experiments required the existence of a second gap about an order of magnitude larger or smaller than the main gap in order to account for certain anomalous features in the data. Many of these features have since been attributed to problems in sample preparation,[36] and are no longer taken as strong evidence for multiple gaps. A critical review of the evidence for anisotropy and multiple gaps in Nb and other materials has been given recently by Bostock and MacVicar.[38] Our data show no evidence for gaps widely separated from the average value but do allow for anisotropy of order 20%. We believe our results are more reliable than those of tunneling, specific heat, or ultrasonic attenuation experiments because our measurements are based on an equilibrium bulk property in well characterized samples. The data are insensitive to impurities, strain, or surface imperfections which affect many of the other experiments for measuring gap anisotropy. In addition, the connection between $\lambda(\mathbf{k})$ and $\Delta(\mathbf{k})$ is simple and direct, leaving little room for error in interpretation.

VI. CONCLUSIONS

We have described a nonrelativistic KKR parametrization of the Fermi surface properties of Nb. Five parameters corresponding to s, p, $d(e_g)$, $d(t_{2g})$, and f phase shifts were fit to ten symmetry direction experimental areas to determine the Fermi-surface geometry. Splitting the d phase shift into t_{2g} and e_g components allows for a nonspherical potential inside the muffin tin spheres. The resulting Fermi-surface geometry agrees very well with all measured features of the Nb Fermi surface. The parametrization shows that the previously unexplained κ, α', and

α'' branches are due to a noncentral orbit on the octahedron and to noncentral breakdown orbits between the octahedron and JG, respectively.

Comparison of the Fermi radii with an empirically adjusted band calculation due to Koelling and Elyashar shows excellent detailed agreement on all three sheets of the surface. We conclude that both the parametrization and the band calculation describe the Fermi-surface geometry very accurately.

The five phase-shift derivatives needed to describe the Fermi velocities were adjusted to fit eight symmetry direction effective masses. Numerical integration of the resulting Fermi velocities predicted an enhanced density of states which agreed with that measured in specific-heat experiments to within 1.2%. This implies that the parametrization scheme correctly describes the enhancements due to electron-phonon interaction and other many-body effects. This conclusion also applies to Au[3], Pt,[5] and Pd.[6,7]

The Fermi velocities from the parametrization were compared to those of the empirically adjusted band calculation of Elyashar and Koelling to derive the anisotropic many-body enhancement $\lambda(\mathbf{k})$. This quantity was found to vary by as much as 60% from sheet to sheet on the Fermi surface, but values within any given sheet were relatively constant. We attribute most of the many-body enhancement to the electron-phonon interaction, though some contribution from the electron-electron interaction cannot be ruled out.[39] Comparison of our derived values for the anisotropy in $\lambda(\mathbf{k})$ with those predicted theoretically shows relatively poor agreement with calculations based on the rigid-muffin-tin approximation and better agreement with tight-binding calculations. The trends in $\lambda(\mathbf{k})$ from sheet to sheet are predicted about equally well by orthogonal tight binding and nonorthogonal tight-binding schemes.

Finally, we use our anisotropic $\lambda(\mathbf{k})$ values to estimate the anisotropy in the energy gap $\Delta(\mathbf{k})$ in Nb. We find no evidence for any gaps widely different from the average gap, though there are variations of about $\pm 10\%$ from sheet to sheet.

ACKNOWLEDGMENTS

We have enjoyed many stimulating discussions with Dale Koelling on several aspects of this work. This work was supported by the U.S. Department of Energy (Office of Basic Energy Sciences, Materials Science Division) under Contract No. W-31-109-ENG-38 and the National Science Foundation under Grant No. DMR-76-21370.

APPENDIX A

The experimental Fermi-surface work on Nb is reported in an unusually wide range of units, including atomic units, Å, and nanometers. We report our results in Brillouin or $2\pi/a$ (bu) units which are the most convenient for the parametrization schemes. In atomic units the unit of length in $\mathbf{k}$ space is the inverse Bohr radius $1/a_0$. In Brillouin units the unit of length is the distance from Γ to H, $2\pi/a$, where a is the lattice constant of Nb, $a=3.295$ Å.

A convenient unit of energy is the energy of a free electron at the H point, $(\hbar^2/2m)(2\pi/a)^2$. The combination of this unit of energy with Brillouin units of length is often called $2\pi/a$ units. Velocities quoted in these units refer to dimensionless values of $\partial E/\partial k$. To convert to laboratory units, these velocities must be multiplied by $\hbar(2\pi/a)/2m = 1.10\times 10^8$ cm/sec for Nb. Through an accident of nature, $\mathbf{k}$ space areas expressed in Brillouin and atomic units are nearly the same for Nb, differing by a factor $(2\pi a_0/a)^2 = 1.0176$.

APPENDIX B

The evaluation of the number of carriers, $n(E)$, and density of states, $N(E)$, for the N-centered and Γ-centered sheets of the surface was accomplished by numerical integration in spherical coordinates using the expressions

$$n(E)=\frac{2}{(2\pi)^3}\tfrac{1}{3}\int k^3\sin\theta\, d\theta\, d\phi \tag{B1}$$

and

$$N(E)=\frac{2}{(2\pi)^3}\int \frac{k^3}{\mathbf{k}\cdot(\partial E/\partial\mathbf{k})}\sin\theta\, d\theta\, d\phi\ , \tag{B2}$$

where here $\mathbf{k}$ is measured from the center. Integration of the N-centered surface involved 90° integration in θ and ϕ relative to the ellipsoid axes, i.e., $\frac{1}{8}$ of the unit sphere; the integrations for the Γ-centered surface, which has full cubic symmetry, involve only $\frac{1}{48}$ of the unit sphere.[2,3] The most difficult integrations involved the open surface and were performed using cylindrical coordinates in the form

$$n(E)=\frac{2}{(2\pi)^3}\tfrac{1}{2}\int k^2 d\phi\, dk_z \tag{B3}$$

and

$$N(E)=\frac{2}{(2\pi)^3}\int \frac{k^2}{\mathbf{k}\cdot(\partial E/\partial\mathbf{k})}d\phi\, dk_z\ , \tag{B4}$$

where k_z is measured along the Γ-H line which we designate $\langle 001\rangle$. The $\frac{1}{48}$ wedge of the zone to be integrated over may be defined by the following four planes

$$\mathbf{k}\cdot\frac{\hat{\mathbf{x}}+\hat{\mathbf{z}}}{\sqrt{2}}=\frac{1}{\sqrt{2}}\ , \tag{B5}$$

$$\mathbf{k}\cdot\hat{\mathbf{y}}=0\ , \tag{B6}$$

$$\mathbf{k}\cdot\frac{\hat{\mathbf{x}}-\hat{\mathbf{y}}}{\sqrt{2}}=0\ , \tag{B7}$$

$$\mathbf{k}\cdot\frac{\hat{\mathbf{x}}-\hat{\mathbf{z}}}{\sqrt{2}}=0\ . \tag{B8}$$

For a given point in the integration defined by ϕ and k_z, one must locate the Fermi surface. If $\mathbf{k}$ is a vector near to both the surface and the desired integration coordinates, then solving the following three linear equations for $\delta\mathbf{k}$ produces a vector $\mathbf{k}'=\mathbf{k}+\delta\mathbf{k}$ which better satisfies these conditions

$$E_F = E(\mathbf{k}) + \frac{\partial E}{\partial \mathbf{k}} \cdot \delta\mathbf{k} \ , \tag{B9}$$

$$\frac{k_y + \delta k_y}{k_x + \delta k_x} = \tan\phi \ , \tag{B10}$$

$$(\mathbf{k} + \delta\mathbf{k}) \cdot \hat{\mathbf{z}} = k_z \ . \tag{B11}$$

The integration over dk_z includes parts of the surface that intersect the zone face or the surface of the primitive wedge; these make a contribution only to the volume integral which may be done analytically by adding contributions $\frac{1}{2}k_\perp^2(1-k_z)$ and $\frac{1}{2}k_\perp^2 k_z$ associated with the planes defined by Eqs. (B5) and (B8), respectively. The quantities $\mathbf{k}_\perp$ and k_z, which define the intersection of the surface with the planes in question, are determined by substituting $\mathbf{k}'$ for $\mathbf{k}$ in Eqs. (B5) and (B8) and using Eqs. (B9) and (B10); this also determines the limits of the remaining numerical part of the dk_z integration.

[1]G. W. Crabtree, W. R. Johanson, S. A. Campbell, D. H. Dye, D. P. Karim, and J. B. Ketterson, in *Physics of Transition Metals 1980,* Inst. Phys. Conf. Ser. No. 55, edited by P. Rhodes (Institute of Physics, Bristol, 1981), p. 79.

[2]G. W. Crabtree, D. H. Dye, D. P. Karim, and J. B. Ketterson, J. Magn. Mag. Mater. **11**, 236 (1979).

[3]J. C. Shaw, J. B. Ketterson, and L. R. Windmiller, Phys. Rev. **5**, 3894 (1972).

[4]J. B. Ketterson, D. D. Koelling, J. C. Shaw, and L. R. Windmiller, Phys. Rev. **11**, 1447 (1975).

[5]D. H. Dye, J. B. Ketterson, and G. W. Crabtree, J. Low Temp. Phys. **30**, 813 (1978).

[6]D. H. Dye, S. A. Campbell, G. W. Crabtree, J. B. Ketterson, N. B. Sandersara, and J. J. Vuillemin, Phys. Rev. **23**, 462 (1981).

[7]W. Joss, L. N. Hall, G. W. Crabtree, J. J. Vuillemin, Phys. Rev. B **30**, 5637 (1984); W. Joss and G. W. Crabtree, *ibid.* **30**, 5646 (1984).

[8]D. P. Karim, J. B. Ketterson, and G. W. Crabtree, J. Low Temp. Phys. **30**, 389 (1978).

[9]D. H. Dye, D. P. Karim, J. B. Ketterson, and G. W. Crabtree, in *Transition Metals 1977,* Inst. Phys. Conf. Ser. No. 39, edited by M. J. G. Lee, J. M. Perz, and E. Fawcett (Institute of Physics, Bristol, 1978), p. 683.

[10]B. N. Harmon and S. K. Sinha, Phys. Rev. B **16**, 3919 (1977).

[11]W. H. Butler, F. J. Pinski, and P. B. Allen, Phys. Rev. **19**, 3708 (1979).

[12]M. Peter, J. Ashkenazi, M. Dacorogna, Helv. Phys. Acta **50**, 267 (1977).

[13]A. L. Simons, C. M. Varma, and W. Weber, Phys. Rev. B **23**, 2431 (1981).

[14]G. W. Crabtree, D. H. Dye, D. P. Karim, D. D. Koelling, and J. B. Ketterson, Phys. Rev. Lett. **42**, 390 (1979).

[15]M. H. Halloran, J. H. Condon, J. E. Graebner, J. E. Kunzler, and F. S. L. Hsu, Phys. Rev. B **1**, 366 (1970).

[16]G. B. Scott and M. Springford, Proc. R. Soc. London Ser. A **320**, 115 (1970).

[17]L. F. Mattheiss, Phys. Rev. B **1**, 373 (1970).

[18]L. L. Boyer, D. A. Papaconstantopoulos, and B. M. Klein, Phys. Rev. B **15**, 3685 (1977).

[19]R. A. Deegan and W. D. Twose, Phys. Rev. **164**, 993 (1967).

[20]R. N. Euwema, Phys. Rev. B **4**, 4432 (1971).

[21]J. R. Anderson, D. A. Papaconstantopoulos, J. W. McCaffrey, and J. E. Schirber, Phys. Rev. B **7**, 5115 (1973).

[22]N. Elyashar and D. D. Koelling, Phys. Rev. B **13**, 5362 (1976).

[23]N. Elyashar and D. D. Koelling, Phys. Rev. B **15**, 3620 (1977).

[24]K. M. Ho, S. G. Louie, J. R. Chelikowsky, and M. L. Cohen, Phys. Rev. B **15**, 1755 (1977).

[25]P. T. Coleridge, Phys. Condens. Matter **19**, 203 (1975).

[26]J. Ferreira da Silva, E. A. Burgemeister, and Z. Pokoupil, Physica (Utrecht) **41**, 409 (1969).

[27]S. K. Sinha, Phys. Rev. **169**, 477 (1968).

[28]G. D. Gaspari and B. L. Gyorffy, Phys. Rev. Lett. **28**, 801 (1972).

[29]C. M. Varma, E. I. Blount, P. Vashishta, and W. Weber, Phys. Rev. B **19**, 6130 (1979).

[30]W. L. McMillan, Phys. Rev. **167**, 331 (1968).

[31]P. B. Allen and R. C. Dynes, Phys. Rev. B **12**, 905 (1975).

[32]W. H. Butler and P. B. Allen, *Superconductivity in d- and f-band Metals,* edited by D. H. Douglass (Plenum, New York, 1976), p. 73.

[33]P. B. Allen, Phys. Rev. B **17**, 3725 (1978).

[34]J. Ashkenazi, M. Dacorogna, and P. B. Allen, Solid State Commun. **36**, 1051 (1980).

[35]D. P. Almond, M. J. Lea, and E. R. Dobbs, Phys. Rev. Lett. **29**, 764 (1972).

[36]G. J. Sellers, A. C. Anderson, and H. K. Birnbaum, Phys. Rev. B **10**, 2771 (1974).

[37]J. W. Hafstrom and M. L. A. MacVicar, Phys. Rev. B **2**, 4511 (1970).

[38]J. L. Bostock and M. L. A. MacVicar, in *Anisotropy Effects in Superconductors,* edited by H. W. Weber (Plenum, New York, 1977), p. 213.

[39]H. Rietschel and H. Winter, Phys. Rev. Lett. **43**, 1256 (1979).